ARL-RP-0597 ● Apr 2017

US Army Research Laboratory

Methods for Analysis and Simulation of Ballistic Impact

by John D Clayton

Reprinted from Recent Patents on Engineering. 2017;11(1):49–61.

NOTICES

Disclaimers

The findings in this report are not to be construed as an official Department of the Army position unless so designated by other authorized documents.

Citation of manufacturer's or trade names does not constitute an official endorsement or approval of the use thereof.

Destroy this report when it is no longer needed. Do not return it to the originator.

ARL-RP-0597 ● Apr 2017

US Army Research Laboratory

Methods for Analysis and Simulation of Ballistic Impact

by John D Clayton
Weapons and Materials Research Directorate, ARL

Reprinted from Recent Patents on Engineering. 2017;11(1):49–61.

REPORT DOCUMENTATION PAGE

Form Approved
OMB No. 0704-0188

1. REPORT DATE *(DD-MM-YYYY)*	2. REPORT TYPE	3. DATES COVERED (From - To)
April 2017	Reprint	October 2016–April 2017

4. TITLE AND SUBTITLE
Methods for Analysis and Simulation of Ballistic Impact

5a. CONTRACT NUMBER

5b. GRANT NUMBER

5c. PROGRAM ELEMENT NUMBER

6. AUTHOR(S)
John D Clayton

5d. PROJECT NUMBER

5e. TASK NUMBER

5f. WORK UNIT NUMBER

7. PERFORMING ORGANIZATION NAME(S) AND ADDRESS(ES)
US Army Research Laboratory
ATTN: RDRL-WMP-C
Aberdeen Proving Ground, MD 21005-5069

8. PERFORMING ORGANIZATION REPORT NUMBER
ARL-RP-0597

9. SPONSORING/MONITORING AGENCY NAME(S) AND ADDRESS(ES)

10. SPONSOR/MONITOR'S ACRONYM(S)

11. SPONSOR/MONITOR'S REPORT NUMBER(S)

12. DISTRIBUTION/AVAILABILITY STATEMENT
Approved for public release; distribution is unlimited.

13. SUPPLEMENTARY NOTES
Reprinted from Recent Patents on Engineering. 2017;11(1):49–61.

14. ABSTRACT
Background: Methods for describing physics of impact and ballistics have been developed over a number of decades. These include analytical mathematical representations as well as modern computer simulations.

15. SUBJECT TERMS
impact physics, materials science, mechanics, terminal ballistics, shock waves

16. SECURITY CLASSIFICATION OF:			17. LIMITATION OF ABSTRACT	18. NUMBER OF PAGES	19a. NAME OF RESPONSIBLE PERSON
a. REPORT	b. ABSTRACT	c. THIS PAGE			John D Clayton
Unclassified	Unclassified	Unclassified	UU	18	19b. TELEPHONE NUMBER (Include area code) 410-278-6146

Standard Form 298 (Rev. 8/98)
Prescribed by ANSI Std. Z39.18

Send Orders for Reprints to reprints@benthamscience.ae

Recent Patents on Engineering, **2017**, *11 (1)*, **49-61**

RESEARCH ARTICLE

Methods for Analysis and Simulation of Ballistic Impact

J.D. Clayton*

Visiting Faculty, Department of Civil Engineering and Engineering Mechanics, Columbia University, New York, NY 10027 USA; A. James Clark School of Engineering, University of Maryland, College Park, MD 20742 USA and Impact Physics, US ARL, Aberdeen, MD 21005-5066 USA

J.D. Clayton

ARTICLE HISTORY

Received: August 31, 2016
Revised: October 23, 2016
Accepted: October 25, 2016

DOI: 10.2174/1872121106661610281602 05

Abstract: ***Background****:* Methods for describing physics of impact and ballistics have been developed over a number of decades. These include analytical mathematical representations as well as modern computer simulations.

Objective*:* Recent and historic developments towards modeling of impact phenomena pertinent to terminal ballistic events are summarized and compared. Two classes of physical problem are of focus: impact and penetration of metallic and/or ceramic targets by projectiles, and propagation of planar shock waves through solid material specimens induced by collision with flyer plates or by explosive loading.

Method*:* The projectile-target problem is analyzed from perspectives of classical hydrodynamics, extensions accounting for strength, and fully resolved explicit dynamics simulations. The planar impact test is studied from perspectives of analytical solutions to Rankine-Hugoniot equations, steady wave analysis, and dynamic finite element simulations of shock waves in material microstructures. Key features of each approach are critically compared.

Results*:* The two classes of physical problem are inherently related since material properties obtained from analysis of the latter experiments are typical input for models of the former problem involving ballistic penetration. Patents to computer methods and ballistic protection systems are noted.

Conclusion*:* Reduced order models are shown to provide efficient, but often approximate, solutions giving insight into general trends. Modern, fully resolved calculations appear to be the only viable route to design and optimization of novel materials or structures with heterogeneous properties or complex geometries.

Keywords: Ballistics, continuum mechanics, shock physics, projectiles, impact, metals, ceramics, crystals.

1. INTRODUCTION

Impact and penetration mechanics are physical phenomena that are of high importance to defense and industrial applications, including those in mining, automotive, and aircraft industries [1, 2]. Furthermore, such phenomena, especially those involving hypervelocity impact, occur in problems relevant to geology and astronomy, *e.g.*, collisions of planetary objects or space debris [3]. The present work is focused on problems in terminal ballistics, encompassing dynamic interactions of projectiles with their intended targets. The purpose of this paper is to categorize and compare various modeling strategies that describe a few characteristic physical problems in terminal ballistics, noting the important features, relative advantages and disadvantages, and key historic and modern references for each strategy. The intent is to provide a useful introductory reference for researchers beginning work in the area, as well as a source of important equations and references for scientists and engineers more experienced in the fields of ballistics and shock physics. However, no attempt is made to cite all relevant works dealing with any given topical area.

Relevance of this work to recent patents in engineering is as follows. This paper covers modeling techniques---formulation of governing differential equations and their analytical or numerical solutions---rather than development of new experimental/diagnostic devices, munitions, or protection systems. Although the content does not directly invoke technologies available in recent patents, it does supplement any such developments of new technologies. A recent patent for finite element computer methods used to obtain numerical solutions for problems involving large

*Address correspondence to this author at the Visiting Faculty, Department of Civil Engineering and Engineering Mechanics, Columbia University, New York, NY 10027 USA; Tel: +1.410.278.6146; Fax +1.410.278.6877; E-mail: jdclayt1@umd.edu; john.d.clayton1.civ@mail.mil

deformations as occurring under impact loading is reported in [4]. Recent patents for ballistic technologies involving armor ceramics and shock mitigation include [5, 6]. Explicit listings of numerous other relevant patents for dynamic protection systems can be found in associated references to industrial and aerospace applications, for example [2, 3].

The first physical problem addressed is impact and penetration of a solid target, typically metallic or ceramic, by a projectile such as a bullet or rod at null obliquity, *i.e.*, the velocity vector of the the projectile is normal to the plane of the impacted surface. A comprehensive book that deals with this problem and related others is [7], including experimental, analytical, and numerical methods of ballistics research. Similar lengthy references dealing with pertinent aspects include [8, 9]. In contrast, the present paper covers only models---analytical and numerical simulations---with experiments noted only in the context of description of the physical problems and validation of the analytical or numerical solutions. Thus, this paper is more concise and focused than these prior works, and it also includes coverage of more recent developments, particularly in areas of dimensional analysis [10, 11, 12, 13] and modern hydrocode simulations [14, 15, 16]. The present description of constitutive models of (poly)crystalline solids, of which projectile and target are comprised, is also more sophisticated than those given in the above-mentioned prior works, accounting for geometric and material nonlinearity [17].

The second physical problem addressed is the response of a (poly)crystalline solid body to dynamic loading by a planar shock wave. A standard method for studying the high pressure constitutive behavior of such a solid is the plate impact test, designed to induce this type of planar shock loading. Both the pressure-volume equation of state (EOS) and the shear strength of the solid can be inferred from results of this test, depending on diagnostics used. Spall fracture [18] properties can also be deduced if the experiment is designed for their interrogation. The EOS, strength, and fracture properties all may enter constitutive models for solids used in hydrocode simulations of terminal ballistic events. A comprehensive and lengthy reference covering experiments and analysis of planar shock loading is [19]. The present work places emphasis on brevity and recent developments in theory, modeling, and simulation. In particular, dynamic finite element simulations of shock propagation and/or spall fracture in polycrystalline microstructures (*e.g.*, [20, 21]) predated by [18, 19] are incorporated herein. Such simulations can be used to relate structure to dynamic properties important for resistance to failure modes incurred during ballistic events, facilitating design of advanced material systems in protection sciences.

For each of the two physical problems noted above, classes of modeling technique are evaluated in terms of flexibility, complexity, and predictive capability. Flexibility, which may also be termed generality, describes the ability of a model to represent a breadth of physical behaviors without fundamentally altering its governing equations. Complexity, *i.e.*, sophistication, of a theory generally reflects how elaborate are the governing equations. Analytical solutions and numerical implementation become more challenging as complexity increases. Finally, predictive capability refers to a model's representation of real physical behavior with minimal calibration. A particular theory is considered more predictive than a competing model if it is able to better depict realistic physics with fewer fitting parameters or ad hoc equations [22, 23].

This paper is organized as follows. Section 2 addresses the ballistic penetration mechanics problem from standpoints of classical hydrodynamic (1-D) analysis, historic and recently extended (yet still reduced order, 1-D) analysis, and modern hydrocode simulations. Section 3 covers the planar shock problem, including analytical solutions to the governing equations for shock in 1-D, steady wave treatments (also 1-D, but usually requiring numerical solutions), and fully resolved explicit dynamic simulations (2-D or 3-D). Each section logically progresses from descriptions of lower to higher sophistication. Conclusions are given in Section 4, including a table summarizing the evaluations of each of the methods.

Important mathematical relations pertinent to each modeling technique are presented throughout. Notation of continuum physics is used, with vectors and tensors written in bold italic font, and scalars and scalar components in italic font. When the index notation is used, the normal summation is implied for repeated indices. Other notation will be clear from context.

2. BALLISTIC IMPACT AND PENETRATION

Models for the mechanics of terminal ballistic events are now presented. In §2.1, the classical 1-D hydrodynamic solution for steady penetration of a semi-infinite body by an eroding projectile is reviewed. In §2.2, extensions to this analysis are discussed, most of which remain 1-D but incorporate finite strength of the target and/or projectile. The modeling techniques discussed in § 2.1 and § 2.2 are necessarily restricted to the particular initial boundary value problem of impact and penetration of a rather long projectile (*e.g.*, a rod or shaped charge jet) into a deep, and therefore confined, target. In contrast, the computational modeling framework presented and evaluated in §2.3 is capable of describing impact events in more complex physical systems, including 2-D (often axisymmetric) and 3-D geometries.

2.1. Hydrodynamic Theory: Classical Analysis

The governing equation for ideal hydrodynamic penetration of a semi-infinite target by a jet or rod is now derived. This derivation will be extended to more sophisticated models in §2.2.

The ideal hydrodynamic theory of penetration of ductile targets by shaped charge jets was reported in the early paper of [24]. The derivation rests on the following primary assumptions: the penetration process is steady-state and one-dimensional (1-D); the target is semi-infinite; the projectile is a continuous jet; and both target and projectile are incompressible with null shear strength, *i.e.*, are effectively ideal fluids.

Denote spatial coordinates at time t by the vector-valued function $\boldsymbol{x} = \boldsymbol{x}(\boldsymbol{X}, t)$, where reference coordinates of a material point are $\boldsymbol{X}$. The particle velocity vector is the time derivative of position:

$$\boldsymbol{\upsilon}(\boldsymbol{X},t)=\frac{\partial \boldsymbol{x}(\boldsymbol{X},t)}{\partial t}. \tag{2.1}$$

Let $\boldsymbol{\sigma}$ denote the symmetric Cauchy stress tensor, and with $\mathrm{tr}(\cdot)$ the trace operator, $p=-\frac{1}{3}\mathrm{tr}\boldsymbol{\sigma}$ is the Cauchy pressure, positive in compression. The spatial mass density is $\rho(\boldsymbol{x},t)$. In the absence of body forces, the local balance of linear momentum in classical continuum mechanics is [17].

$$\nabla\cdot\boldsymbol{\sigma}=\rho\dot{\boldsymbol{\upsilon}}, \tag{2.2}$$

where the superposed dot is a material time derivative and where $\nabla(\cdot)$ is the gradient with respect to spatial coordinates. The particle acceleration is

$$\dot{\boldsymbol{\upsilon}}(\boldsymbol{x},t)=\frac{\partial \boldsymbol{\upsilon}(\boldsymbol{x},t)}{\partial t}+\nabla\boldsymbol{\upsilon}(\boldsymbol{x},t)\cdot\boldsymbol{\upsilon}(\boldsymbol{x},t). \tag{2.3}$$

Under the aforementioned assumption of steady flow, $\boldsymbol{\upsilon}(\boldsymbol{x},t)\rightarrow\boldsymbol{\upsilon}(\boldsymbol{x})$, and the first term on the right side of (2.3) vanishes, leading to

$$\dot{\boldsymbol{\upsilon}}(\boldsymbol{x})=\nabla\boldsymbol{\upsilon}(\boldsymbol{x})\cdot\boldsymbol{\upsilon}(\boldsymbol{x}). \tag{2.4}$$

For steady 1-D flow, (2.2) becomes, with $\sigma(x)=-\sigma_{11}(x)$ the axial stress, taken here as positive in compression,

$$-\frac{1}{\rho}\frac{\mathrm{d}\sigma}{\mathrm{d}x}=\upsilon\frac{\mathrm{d}\upsilon}{\mathrm{d}x}\Rightarrow-\mathrm{d}\sigma=\rho\upsilon\mathrm{d}\upsilon. \tag{2.5}$$

Conservation of mass requires

$$\dot{\rho}=\rho\nabla\cdot\boldsymbol{\upsilon}. \tag{2.6}$$

For incompressible flow, $\rho[\boldsymbol{x}(\boldsymbol{X},t),t]=\rho[\boldsymbol{x}(\boldsymbol{X})]$.

The physical problem is now analyzed by assuming that an incompressible jet or rod with initial velocity V strikes the target, an incompressible and infinite half-space. The stagnation point between projectile and target recedes with a velocity of magnitude U. The axial stress P at the stagnation point in the projectile is obtained by integrating (2.5), with ρ_0 the constant projectile density, leading to [25]

$$-\int_0^P\mathrm{d}\sigma=\rho_0\int_{V-U}^0\upsilon\mathrm{d}\upsilon\Rightarrow P=\frac{1}{2}\rho_0(V-U)^2. \tag{2.7}$$

Now considering the stagnation point in the target with mass density ρ_T,

$$-\int_0^P\mathrm{d}\sigma=\rho_T\int_U^0\upsilon\mathrm{d}\upsilon\Rightarrow P=\frac{1}{2}\rho_T U^2. \tag{2.8}$$

Finally, P from (2.7) is set equal to P from (2.8), and under the assumption of inviscid flow (no shear stress), $p=P$. The result is Bernoulli's equation for steady hydrodynamic penetration:

$$p=P=\frac{1}{2}\rho_0(V-U)^2=\frac{1}{2}\rho_T U^2. \tag{2.9}$$

The time needed from first impact for a projectile of initial length L_0 to fully erode is $t_0=L_0/(U-V)$, and the final depth of penetration is $P_0=U\cdot t_0$. From (2.9), the normalized depth of penetration can be obtained in terms of the ratio of constant mass densities of the target and projectile materials:

$$\frac{P_0}{L_0}=\frac{U}{U-V}=\sqrt{\frac{\rho_0}{\rho_T}}. \tag{2.10}$$

The original intended subject of this equation was penetration of ductile metallic targets by ductile metallic jets, as in [24]. Subsequently, and often with some degree of success, (2.9) and (2.10) have been invoked to describe the steady penetration regime for long-rod projectiles (typically of high density and metallic origin) as well as brittle targets (*e.g.*, ceramics). The advantage of this simple model is that it requires no fitting parameters whatsoever for the substances: only their density ratio need be known. The disadvantage is that it fails to account for effects of finite strength (*i.e.*, shear stresses) and finite compressibility of either the projectile or the target, both of which may become important depending on the true geometry of the target and projectile, the materials involved, and the striking velocity. However, the ideal hydrodynamic solution provides a useful limiting case for comparisons with test data and for comparisons with more sophisticated analytical or numerical calculations.

2.2. Hydrodynamic Theory: Extensions

A vast number of 1-D analytical penetration mechanics theories have been based on extensions of the ideal hydrodynamic solution derived in §2.1. Several notable such models, termed reduced order theories, are now discussed in this work.

Birkhoff *et al*. [24] modified the hydrodynamic theory to allow for jet particulation by using a shape factor λ that has a value of unity for continuous jets and a value of two for dispersed particle jets:

$$\lambda\rho_0(V-U)^2=\rho_T U^2\Rightarrow\frac{P_0}{L_0}=\sqrt{\frac{\lambda\rho_0}{\rho_T}}. \tag{2.11}$$

Pack and Evans [26, 27] extended the solution in (2.10) to allow for secondary penetration, *i.e.*, after-flow in addition to primary penetration, r. These authors also included an empirical correction for nonzero target strength Y_T:

$$\frac{P_0}{L_0}=\sqrt{\frac{\lambda\rho_0}{\rho_T}}\left(1-a\frac{Y_T}{\rho_0V^2}\right)+\frac{r}{L_0}. \tag{2.12}$$

In this theory, the scalar function a is permitted to depend on target and jet densities, and $aY_T/(\rho_0V^2)=kR$, with k an empirical factor and R the work per unit volume required for crater formation. Eichelberger [28] added to (2.9) an empirical statistical correction parameter γ, and also incorporated the net strength difference $Y_N=Y_T-Y_0$, with Y_0 the jet/projectile strength:

$$\gamma\rho_0(V-U)^2=\rho_T U^2+2Y_N. \tag{2.13}$$

Not long thereafter, Alekseevski [29] and Tate [30] developed theories for long-rod penetration of ductile metallic targets that addressed non-steady behavior, specifically deceleration of the rod due to finite strengths of the projectile (Y_0) and the target (R_T). The governing equation for equal stresses in target and projectile at the stagnation point is obtained in this approach by modifying the limits of integration in (2.7) and (2.8) such that steady

flow does not commence until the stress reaches the resistance of either material:

$$-\int_{Y_0}^{P} \mathrm{d}\sigma = \rho_0 \int_{V-U}^{0} v\mathrm{d}v \Rightarrow P = \tfrac{1}{2}\rho_0 (V-U)^2 + Y_0; \quad (2.14)$$

$$-\int_{R_T}^{P} \mathrm{d}\sigma = \rho_T \int_{U}^{0} v\mathrm{d}v \Rightarrow P = \tfrac{1}{2}\rho_T U^2 + R_T. \quad (2.15)$$

Axial stresses P are equated, which gives Tate's extended Bernoulli equation:

$$\tfrac{1}{2}\rho_0 (V-U)^2 + Y_0 = \tfrac{1}{2}\rho_T U^2 + R_T. \quad (2.16)$$

The complete theory developed in [29, 30] includes differential equations for projectile deceleration and erosion that must be integrated to obtain depth of penetration. Exact solutions have been reported in [31]. If deceleration is ignored, then the analytical solution for penetration depth is

$$\frac{P_0}{L_0} = \frac{U}{U-V} = \frac{1}{\mu}\left(\frac{\mu\sqrt{V^2+A}-V}{\mu V-\sqrt{V^2+A}}\right), \quad (2.17)$$

where

$$\mu = \sqrt{\rho_T/\rho_0},\ A = 2(1-\mu^2)(R_T - Y_0)/\rho_T. \quad (2.18)$$

The equivalent steady state solution can be recovered from (2.13) when $\gamma \to 1$ and $Y_N \to R_T - Y_0$. Importantly, reduces to the hydrodynamic result (2.10) for very high velocities or low material strengths, *i.e.*, when $V^2 >> A$. Analytical predictions are compared with numerical results for metal rods penetrating metal targets in [32]. Such comparisons show that target resistance R_T depends on the experimental configuration (*e.g.*, geometry) in addition to the target material's properties, implying that generally $R_T \neq Y_T$.

Walker and Anderson [33] derived a time-dependent analytical-numerical technique to model unsteady long-rod penetration of semi-infinite targets. This approach considers initial impact, requiring an initial interface velocity from the shock jump conditions that will be reviewed later in §3.1, as well as rod deceleration. Key assumptions are invoked regarding the plastic flow field in the target, obtained from a dynamic cavity expansion analysis, and regarding the velocity profile in the projectile, obtained from a priori numerical simulation. For a limiting case, the analogy of Tate's target resistance was found to vary with the dynamic ratio β of plastic zone size to cavity size:

$$R_T = \tfrac{7}{3} Y_T \ln[\beta(V)]. \quad (2.19)$$

Dimensional analysis of simulation results [34] for metals showed that larger-scale targets tend to be weaker than their small-scale counterparts due to rate and time-to-failure effects. This size effect arises since longer times are available for damage mechanisms such as cracks and shear localization zones to incubate and propagate in larger targets. Similar size effects have also been observed in layered ceramic-metal targets [35]. Experiments and hydrocode simulations were used to probe the importance of strengths of both target and projectile over a range of impact velocities in [36]. Strength effects were found to decrease with increasing impact velocity, lending credibility to the limiting Bernoulli solution (2.10) in the extreme hypervelocity regime. Simulation results likewise showed a small effect of compressibility on penetration for very ductile metallic targets [37]. However, compressibility becomes more important in ceramic targets and concrete, for example, wherein initial porosity decreases with increasingly high compressive pressure, and where strength and pressure are coupled in the constitutive response due to frictional effects, for example [38, 39, 23].

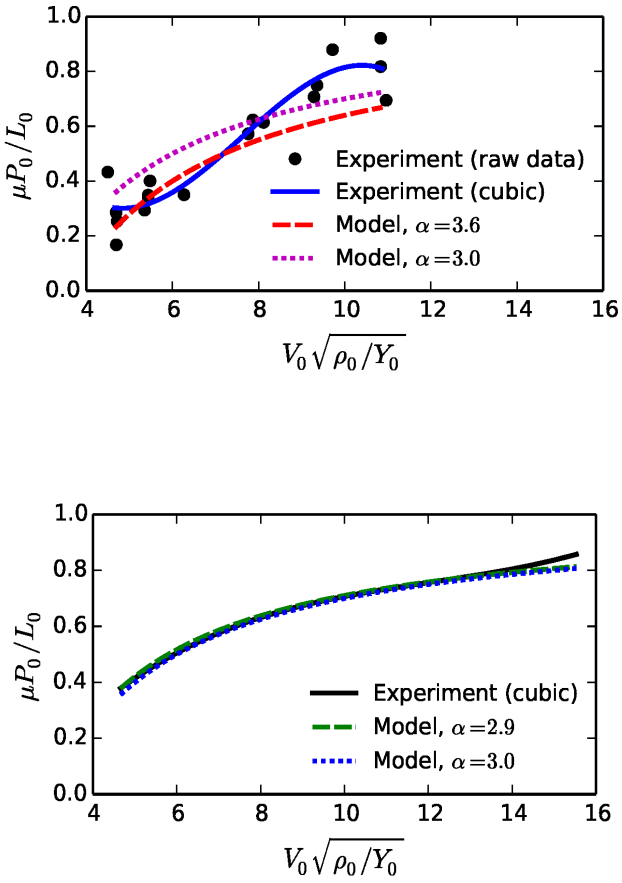

Fig. (1). Extended hydrodynamic theory based on dimensional analysis applied to aluminum oxide (top) and boron carbide (bottom) [11].

Methods of dimensional analysis have been used to provide further insight into parameters and properties affecting the ballistic response of metallic [12, 13] and ceramic [10, 11] targets. The treatment in [11] is considered in further detail in what follows next. The penetration depth equation derived therein from dimensional and physical considerations is, with α_i fitting parameters that potentially depend on the target material:

$$\frac{P_0}{L_0} = \frac{1}{\mu}\left(\alpha_0 + \alpha_1 \frac{\sqrt{Y_0/\rho_0}}{V_0} + \cdots\right) \approx \frac{1}{\mu}\left(1 - \alpha \frac{\sqrt{Y_0/\rho_0}}{V_0}\right), [\alpha_0 = 1; \alpha_1 = -\alpha]. \quad (2.20)$$

This equation was applied to experimental penetration data of [40, 41, 42, 43] where target materials encompassed

the following polycrystalline ceramics: aluminum oxide, aluminum nitride, boron carbide, and silicon carbide. All experiments were conducted in reverse mode [7], with long-rod hypervelocity impact and penetration into confined cylindrical ceramic targets. Projectiles were relatively pure polycrystalline tungsten. Impact velocities V_0 range from 1.5 to 5.0 km/s. The primary discovery reported in [11] is that normalized penetration data for all four ceramic target materials can be described well using (2.20) truncated at $\alpha_1 = -\alpha$, with a single fitting parameter, α, taking a universal value of 3.0. Characteristic results are shown in Fig. **1** for alumina and boron carbide, wherein best fits of α provide little improvement over the universal value of 3. With α thus found independent of target material, penetration depth depends only on the properties of the projectile (Y_0 and ρ_0) and the density of the target entering the factor $\mu = \sqrt{\rho_T/\rho_0}$. Thus, static and dynamic strength properties and underlying mechanisms would seem to be of little influence on penetration depth for this test configuration, since otherwise α would tend to vary among the targeted materials. In future work, parametric numerical simulations of the sort discussed later in § 3.3, wherein material properties can be varied systematically should provide further insight into the origin of α for polycrystalline ceramics.

Comparison of results in [11] with another dimensional analysis [10] of a different target configuration and velocity regime is instructive. This different problem geometry, as explained in [7, 44, 45] for example, consists of one or more ceramic tiles backed by a semi-infinite ductile metal block. Performance of the ceramic is measured by the depth of penetration of the projectile into the backing metal. In [10], dimensional analysis determined that penetration of relatively thin, metal-backed ceramic tiles could be described by two parameters that depend on the type of ceramic material. One parameter is needed to represent the effect of tile thickness. Analysis in [10] found it to be associated with the ratio of fracture surface energy to elastic modulus. The second parameter describes the relationship between penetration depth and impact velocity and appears to be related to the ratio of dynamic shear strength to target density. Comparison of the dimensional analyses in the two papers [10, 11] reveals an apparent transition from fracture- and dynamic strength-controlled resistance to mass density-controlled resistance with increasing impact velocity and increasing target thickness or confinement.

The reduced order models discussed above in § 2.2 present the following positive features. Effects of strength of the projectile and target can be included in the analysis with relatively little increase in model complexity. Such effects are often important for lower striking velocities, thinner targets, or for stiff materials such as ceramics. Solutions are relatively easy to obtain, either analytically or via numerical quadrature. Drawbacks are that the models remain one-dimensional, such that effects of lateral boundaries associated with finite sized projectile and target configurations are omitted. Furthermore, parameters entering such models are usually calibrated to match observed trends or hydrocode simulation results, rather than obtained from first principles or fundamental experiments on constitutive behavior. In this sense, the reduced order models tend to be prescriptive rather than predictive, though comparison of calibrated parameters for different materials subjected to similar loading conditions may give qualitative insight into underlying physical phenomena.

2.3. Hydrocode Simulations

Unlike the 1-D models reported in § 2.1 and § 2.2, computer simulations enable depiction of complex penetrator-target geometries, *i.e.*, those requiring 2-D or 3-D representations. The software used to solve the governing equations of continuum dynamics is termed here a hydrocode, though the materials involved need not be perfectly hydrodynamic. In other words, shear stresses are admitted in addition to pressure p, or the stress tensor $\boldsymbol{\sigma}$ need not be isotropic. An early summary of hydrocode simulations can be found in [9]. The forthcoming presentation covers more advanced topics with a focus on nonlinear continuum mechanics principles, including finite deformations and nonlinear material models.

The class of models discussed next accounts for large strains and rotations, as both may occur during deformation of ductile metals [17, 46], and even in ceramics and minerals when loading is predominantly compressive [47, 48]. Only the essential equations are provided, and Cartesian coordinates are implied when index notation is used. For a more comprehensive treatment that encompasses curvilinear coordinates, see [17], with general kinematics addressed in more detail in [49]. Governing equations of finite anisotropic elasticity are also given in [50, 51].

The forthcoming presentation considers a (poly)crystalline solid such as a metal or ceramic material. Under conditions of ballistic impact, the material may degrade in strength, *i.e.*, undergo a damage process. In the present framework, local damage is represented by a scalar state variable $D(\boldsymbol{X}, t) \in [0, 1]$. Generalization to a vector, tensor, or multiple scalars is possible but not undertaken here to maintain a terse review. The solid is assumed to be hyperelastic and may undergo plastic slip.

Spatial coordinates of a deformable body are related to material coordinates by the time dependent motion

$$\boldsymbol{x} = \boldsymbol{x}(\boldsymbol{X}, t) = \boldsymbol{X} + \boldsymbol{u}(\boldsymbol{X}, t), \tag{2.21}$$

where $\boldsymbol{u}$ is the displacement vector. The deformation gradient is decomposed in multiplicative form as

$$\boldsymbol{F} = \nabla_0 \boldsymbol{x} = \boldsymbol{F}^E \boldsymbol{F}^D \boldsymbol{F}^P, \tag{2.22}$$

where $\boldsymbol{F}^E$ includes thermoelastic deformation and mechanically reversible changes in damage (*e.g.*, elastic crack closure on load release), $\boldsymbol{F}^P$ accounts for plastic slip from dislocations, and $\boldsymbol{F}^D$ accounts for mechanically irreversible damage mechanisms like cracks and voids that remain after local elastic unloading. A three term decomposition of this general form was proposed in [52]. Other deformation gradient representations that account for damage explicitly include additive [53, 54, 55] and hybrid additive-multiplicative [56, 57] forms, often derived or motivated from homogenization of discrete displacement jumps due to subscale cracks within a volume element. The

volume fraction of damage Ξ is related to the determinant of $\boldsymbol{F}^D$:

$$\det\boldsymbol{F}^D = (1-\Xi)^{-1/3}. \tag{2.23}$$

Besides its use for solids with voids [58, 52] or pores [38, 23] a multiplicative damage term has been introduced for cleavage cracking in crystals of metallic, mineral, or ceramic origins [39, 59, 48]

The local balance laws of continuum mechanics, in spatial form, consist of the conservation of mass, linear momentum, and energy:

$$\dot{\rho} = \rho\nabla\cdot\boldsymbol{\upsilon},\ \nabla\cdot\boldsymbol{\sigma}+\boldsymbol{f} = \rho\dot{\boldsymbol{\upsilon}},\ \rho\dot{e} = \boldsymbol{\sigma}\colon\nabla\boldsymbol{\upsilon} - \nabla\cdot\boldsymbol{q}. \tag{2.24}$$

The body force vector is $\boldsymbol{f}$, the internal energy per unit mass is e, and the spatial heat flux vector is $\boldsymbol{q}$. Symbols for density, velocity, and stress are the same as those introduced in §2.1. The local balance of angular momentum is not solved explicitly, and simply requires that the stress tensor $\boldsymbol{\sigma}$ be symmetric. Point heat sources are not relevant for the present scope and are omitted from the energy balance. Hydrocode simulations integrate the coupled governing partial differential equations in (2.24) in time and space, given boundary and initial conditions. The equations in (2.24) alone are insufficient: a constitutive model is required for each material, providing the mathematical relationships among stress, internal energy, the deformation gradient, and the latter's history and rate.

The thermoelastic strain used in standard crystal hyperelasticity [17, 50] is the Green strain tensor:

$$\boldsymbol{E} = \tfrac{1}{2}[(\boldsymbol{F}^E)^{\mathrm{T}}\boldsymbol{F}^E - \boldsymbol{1}],\ E_{IJ} = \tfrac{1}{2}(F^E_{kI}F^E_{kJ} - \delta_{IJ}). \tag{2.25}$$

The thermoelastic volume change is measured by $J^E = \det\boldsymbol{F}^E$. Other more recent formulations have used other strain tensors, including Eulerian and logarithmic tensors referred to material coordinates, with improvements over the Green strain representation for metals, ceramics, and minerals [47, 60, 48, 61, 62] Substitution of $\boldsymbol{E}$ with one of these alternative strain tensors is relatively straightforward. Herein, following the standard approach, Cauchy stress $\boldsymbol{\sigma}$ is related to elastic second Piola-Kirchhoff stress $\boldsymbol{S}$ *via*

$$\boldsymbol{\sigma} = \tfrac{1}{J^E}\boldsymbol{F}^E\boldsymbol{S}(\boldsymbol{F}^E)^{\mathrm{T}},\ \sigma_{ij} = \tfrac{1}{J^E}F^E_{iK}S_{KL}F^E_{jL}. \tag{2.26}$$

An internal energy function per unit mass, with corresponding temperature-entropy relation, is

$$e = e(\boldsymbol{E},\eta,\{\xi\}) = e(\boldsymbol{E},\eta,\rho_D,D,\dots),\ T = \partial e/\partial\eta. \tag{2.27}$$

with $\{\xi\}$ a set of internal state variables that affect the energy stored in the solid, *e.g.*, dislocation density ρ_D and damage D. This damage variable D presumably varies from zero to unity as the material at the corresponding point loses integrity. The thermoelastic stress-strain relation for an arbitrary anisotropic hyperelastic solid is

$$S_{IJ} = J^E\rho\frac{\partial e}{\partial E_{IJ}} = C_{IJKL}E_{KL} + \tfrac{1}{2!}C_{IJKLMN}E_{KL}E_{MN} + \tfrac{1}{3!}C_{IJKLMNPQ}E_{KL}E_{MN}E_{PQ} + \cdots - T_0\Gamma_{IJ}\Delta\eta - \cdots, \tag{2.28}$$

where $C_{IJKL\dots}$ are isentropic elastic coefficients of second- and higher orders, $\Delta\eta$ is entropy change measured from a reference state at temperature T_0, and Γ_{IJ} are Grüneisen coefficients. Elastic moduli depend on damage. The simplest degradation model of the moduli is linear in D:

$$\boldsymbol{C}[D(\boldsymbol{X},t),\boldsymbol{X}] = [1-D(\boldsymbol{X},t)]C_0(\boldsymbol{X}), \tag{2.29}$$

with $\boldsymbol{C}_0(\boldsymbol{X}) = \boldsymbol{C}(0,\boldsymbol{X})$ the tensor of elastic moduli for the undamaged (poly)crystal at the corresponding material point. More sophisticated approaches are needed to realistically capture physics of arbitrary loading cycles, *e.g.*, such as damage induced anisotropy and differences in tensile and compressive degradation.

The viscoplastic flow rule is often of the general form

$$\dot{\boldsymbol{F}}^P = \dot{\boldsymbol{F}}^P(\boldsymbol{S},T,\{\xi\},\boldsymbol{F}^P), \tag{2.30}$$

where $\boldsymbol{S}$ can be replaced with the most appropriate stress tensor for the corresponding configuration space. Kinetic equations must likewise be supplied for time rates of $\boldsymbol{F}^D$ and internal state variables, for example

$$\dot{\boldsymbol{F}}^D = \dot{\boldsymbol{F}}^D(\boldsymbol{E},\eta,\{\xi\},\boldsymbol{F}^D),\ \{\dot{\xi}\} = \{\dot{\xi}\}(\boldsymbol{E},\eta,\{\xi\}). \tag{2.31}$$

Dependence on elastic strain, entropy, and internal state variables is perhaps more physically meaningfully substituted with dependence on stress, temperature, and conjugate thermodynamic driving forces. The local balance of energy in the last equation in (2.24), for adiabatic conditions often appropriate in impact dynamics, can be expressed as a temperature rate equation:

$$\dot{T} = \frac{\beta(\{\xi\})}{c}\dot{W} - T\boldsymbol{\Gamma}\colon\dot{\boldsymbol{E}}, \tag{2.32}$$

where c is the specific heat per unit volume at constant thermoelastic strain, $\dot{W}$ is the dissipated energy rate from plasticity and damage mechanisms, and β is the fraction of dissipation converted to heat energy, *i.e.*, the fraction of stored energy of cold work is $1-\beta$. Theory and simulations, including a representative result in Fig. **4** of [14], have demonstrated links among microstructure (*e.g.*, dislocation density), stored energy of cold working, and ballistic penetration resistance of metallic targets (see also [15]).

In addition to the governing partial differential equations for the bulk response of materials, physics-based model representations of contact between impacted bodies must be introduced, accounting for momentum transfer and possible frictional effects. Furthermore, means for addressing complete failure of the material in numerical frameworks become essential since element distortions, if too large, render Lagrangian finite elements inaccurate. Perhaps the simplest such method is finite element deletion, where a given element is suitably eliminated from the calculation when its strength vanishes [63]. This approach, unfortunately, does not always ensure that all conservation laws of (2.24) are obeyed consistently upon failure. Another approach involves conversion of Lagrangian finite elements to interacting particles when large strain thresholds associated with failure are attained [64]. Results of a simulation invoking this approach, specifically addressing dynamic fragmentation of concrete targets, are shown in Fig.

10 of [38]. Other more recent methods such as extended finite elements (X-FEM) [63, 65] and discrete element methods [66], which even if less prevalent in hydrocodes, may better satisfy the conservation laws and thus allow for a more realistic description of dynamic fracture and fragmentation.

Relative to hydrodynamic theory and its extensions discussed in §2.1 and §2.2, hydrocode simulations offer many advantages. As noted already, complex geometries can be resolved, for example heterogeneous, layered targets of finite dimensions [67, 16]. Stress wave interactions can be visualized via modern post-processing tools. Material behavior can be sophisticated and realistic, with nonlinear constitutive models of the sort discussed above enabled. The primary disadvantage of hydrocode modeling is the cost. Firstly, the code or software must be obtained or written, the latter an imposing endeavor requiring expertise in continuum physics and computer science. Secondly, solutions to most impact problems are computationally expensive, with cost tending to increase with model complexity, both geometric and material. Time step size for explicit integration is restricted by the Courant condition, which limits the total time duration over which the momentum equations can be integrated. In other words, impact events can only be simulated over short time periods. The maximum time step size becomes smaller for finer meshes and stiffer materials, making simulations of small and stiff structures very expensive. Finally, constitutive models for the material response may require calibration, ideally via comparison with data from fundamental experiments rather than matching to ballistic data. The latter situation is sometimes unavoidable, however, depending on availability of test data and/or any deficiencies in the physical model for the material.

3. PLANAR SHOCK WAVES

Methods for modeling the response of solids subjected to shock wave propagation, typically induced by planar impact, are now addressed. In §3.1, the classical sharp interface treatment of a steady planar shock passing through a homogeneous material is reviewed, with the Rankine-Hugoniot jump conditions the primary results. For relatively simple kinds of constitutive laws, the 1-D equations can be solved simultaneously and analytically, though not always in closed form. In §3.2, another 1-D treatment is presented for analysis of planar shock waves, where steady state behavior is presumed, but the shock width is finite and is an outcome of the analysis. The computational methods of §3.3 resolve transient details of the shock as it travels through heterogeneous microstructures. Of keen interest is the predicted response of polycrystalline materials pertinent to munitions (metals) and armors (ceramics) often featured in ballistic applications of §2.

3.1. Hugoniot Jump Conditions and Analytical Solutions

The present analytical approach to modeling planar shocks in metals, ceramics, and geologic materials involves simultaneous solution of the Rankine-Hugoniot jump conditions for conservation of mass, momentum, and energy, along with constitutive equations for the physical behavior of the particular material system. Constitutive laws may be elastic, elastic-plastic, or elastic-plastic with damage. The onset of inelastic response corresponds to the Hugoniot Elastic Limit (HEL); shocks of strength at or exceeding this value induce irreversible deformation mechanisms such as slip, twinning, pore collapse, and/or fracture.

For elastic-plastic single crystals, the technique described here and in [68] can be applied only for high symmetry orientations: for example shocks propagating along [100] and [111] directions in FCC and BCC crystals or along [0001] directions in HCP crystals. Such symmetries reduce the problem to simultaneous solution of a yield condition and energy balance for the cumulative plastic slip and entropy, with the remaining conservation and constitutive laws sufficient for determination of the downstream material state. Downstream refers to material behind the plastic shock wave, and upstream to material ahead of the shock. For lower symmetry geometries, transverse waves would appear, and the 1-D description would be an approximation, often severe.

Considered is a planar shock moving at natural velocity D in the Lagrangian direction X, across which velocity, stress, and deformation gradient are discontinuous. Let $(\cdot)^+$ and $(\cdot)^-$ denote values of a quantity upstream and downstream from the shock. The jump of a quantity across the shock plane is then

$$[[\cdot]] = (\cdot)^- - (\cdot)^+. \tag{3.1}$$

Denote by $\mathrm{v} = v - D$ the velocity of the material relative to the shock front, with v the particle velocity for 1-D motion. The Cauchy stress component normal to the front is equal to the negative of the shock pressure: $\sigma = -P$. The internal energy per unit mass is e, the mass density ρ. Then the Rankine-Hugoniot equations for a steady planar shock are written as the following jump conditions for mass, linear momentum, and energy [69]:

$$\big[[\rho \mathrm{v}]\big] = 0, \big[[\sigma]\big] - \rho \mathrm{v}\big[[\mathrm{v}]\big] = 0, [[\rho \mathrm{v}(e + \mathrm{v}^2/2) - \sigma \mathrm{v}]] = 0. \tag{3.2}$$

The deformation gradient is uniaxial, *i.e.*, $\boldsymbol{F} = \mathbf{1} + (\partial u/\partial X)\boldsymbol{n} \otimes \boldsymbol{n}$, where $\boldsymbol{n}$ is a unit vector in the direction of motion X and $u(X,t)$ the displacement component in this direction. The above system of equations becomes closed upon prescription of the constitutive model relating uniaxial deformation gradient, internal energy, and stress components. Such constitutive models belong to the general class of theories outlined in §2.3, and for elastic-plastic single crystals, those further elaborated in §3.3.

Closed form analytical solutions have been derived for ideal cases. Perfectly compressible fluids were analyzed in [70]. A solution valid for nonlinear elastic, anisotropic crystals or polycrystals incorporating the Green strain of (2.25) is presented in [50]. Analytical solutions for anisotropic single crystals in the context of (material) Eulerian strain and logarithmic strain were first derived in [47] and [48], respectively. Subsequent evaluation of solutions versus shock data for a number of single crystals [60, 62] determined that Eulerian theory is often most accurate for ductile metals, while logarithmic theory is

preferred for strong ceramics with a relatively high ratio of shear to bulk modulus.

Analytical solutions can also be obtained, not necessarily in closed form, for materials undergoing inelastic behavior such as plastic slip. Isotropic elastic-plastic solids were addressed in [69, 71]. More recently, incremental analytical methods have been developed to account for multiple yield limits in isotropic polycrystals, as shown in Fig. **1** of [72] for the ceramic titanium diboride. Anisotropic elastic-plastic single crystals have been addressed in [48, 68]. In this case, the aforementioned restrictions on symmetry with respect to shock propagation direction apply, and inelastic deformation is of the form

$$\boldsymbol{F}^P(\gamma) = \exp(\gamma \sum_\alpha \boldsymbol{s}^\alpha \otimes \boldsymbol{m}^\alpha) = \boldsymbol{1} + \gamma \sum_\alpha \boldsymbol{s}^\alpha \otimes \boldsymbol{m}^\alpha + \frac{1}{2}\gamma^2(\sum_\alpha \boldsymbol{s}^\alpha \otimes \boldsymbol{m}^\alpha)^2 + \frac{1}{6}\gamma^3(\sum_\alpha \boldsymbol{s}^\alpha \otimes \boldsymbol{m}^\alpha)^3 + \cdots. \quad (3.3)$$

The cumulative shear γ thus encompasses the entire deformation history in a single kinematic parameter. The slip direction and slip plane normal vectors for system α are $\boldsymbol{s}^\alpha$ and $\boldsymbol{m}^\alpha$. A one parameter model for strength is also typically prescribed, though history effects can be admitted without much more complexity [48]. Results of this type of analysis are shown in Fig. **5** of [48] for single crystal diamond shocked along a cube axis, a very strong solid which could undergo slip or cleavage on its octahedral planes when shocked above its HEL.

Advantages of the method of analysis described here in §3.1 include relative simplicity: few material parameters are needed, and solutions are obtained nearly instantly. The method is flexible enough to incorporate various nonlinear anisotropic thermoelastic potentials. Disadvantages are that only isotropic solids or highly symmetric orientations can be modeled and time dependent effects such as viscosity (*e.g.*, explicit strain rate effects on strength) are omitted. Finally, because shock is treated as a perfect jump discontinuity, no information regarding its structure such as shock width or values of state variables within the shock front is obtained. While only a single fitting parameter may be required as in [68], its value must still be prescribed via comparison with shear strength data from experiments or results of an independent model of material response.

For materials undergoing inelastic response, this class of models can be used effectively and efficiently to probe possible underlying mechanisms such as slip, cleavage, twinning, and pore collapse by analyzing various orientations and comparing theoretical yield criteria with test data [73, 74, 75]. The resulting information can be used to inform equations or parameters of more sophisticated material models such as those invoked in steady wave or fully resolved finite element calculations of §3.2 and §3.3. Furthermore, a model can be developed for one orientation or symmetry by calibrating to test data then used to predict behavior for another configuration for which data may be unavailable [23].

3.2. Steady Wave Solutions

The steady wave class of modeling shock waves involves transformation of governing partial differential equations of dynamic continuum mechanics to ordinary differential equations relative to a coordinate frame that moves along with a steady (*i.e.*, constant velocity) wave. The steady wave method has been invoked to study plastic shocks in isotropic solids in [76, 77]. The first theory and application of the method towards anisotropic elastic-plastic crystals were described in [78], with supplementary studies involving this method as well as finite difference simulations reported in [79, 80, 68].

The system of equations whose simultaneous solution is sought in a steady wave analysis consists of the following continuity and momentum conservation laws [68]:

$$\frac{\mathrm{d}v}{\mathrm{d}Y} = -D\frac{\mathrm{d}\lambda}{\mathrm{d}Y},\ \frac{\mathrm{d}P}{\mathrm{d}Y} = \rho_0 D\frac{\mathrm{d}v}{\mathrm{d}Y}. \quad (3.4)$$

The shock velocity is D, and $Y = X - Dt$ is a coordinate moving with steady velocity in the direction X of shock propagation. The deformation is again presumed uniaxial, *i.e.*, $\boldsymbol{F} = \boldsymbol{1} + (\partial u/\partial X)\boldsymbol{n} \otimes \boldsymbol{n}$ as in § 3.1, and $\lambda = 1 + \partial u/\partial X$ is the axial compression ratio. The system of equations also includes those of the constitutive model, which falls into the classes described in §2.3, and may be of any degree of sophistication so long as symmetry respects the unaxial kinematic condition. Time differentiation entering kinetic equations for the constitutive model is transformed to differentiation with respect to the moving coordinate Y. In general the coupled system of governing ordinary differential equations must be integrated numerically. This contrasts the less advanced material models for which analytical solutions to jump conditions are restricted in § 3.1. For certain simple cases of isotropic material response, analytical solutions to the continuous steady wave problem may be possible [76].

Advantages of the steady wave method include the following: a detailed description of the steady shock structure is obtained, solutions are obtained at relatively low computational cost, no artificial viscosity is used (unlike many finite difference and finite element simulations of strong shocks), and sophisticated rate- and temperature-dependent constitutive models are enabled. An example of achievable results is shown in Fig. **11** of [78], which demonstrate effects of lattice orientation and shock pressure on shock width in aluminum. The assertion of low computational expense has been verified via comparison with (more lengthy) finite difference simulations of the same physical problem [68]. The computational efficiency of the steady wave method facilitates its role as a tool for investigating and parameterizing advanced constitutive models for subsequent use in more expensive, fully resolved simulation frameworks.

Disadvantages result from the symmetry and steadiness restrictions. Accordingly, effects of transverse waves for non-symmetric crystal orientations are ignored, unsteady waves cannot be addressed, and material properties must be spatially homogeneous. Only fully resolved simulations such as finite difference calculations or explicit finite element simulations of the class described next in §3.3 are capable of quantifying transient aspects of evolving shock waves. Important transient effects include elastic precursor decay and wave interactions, *e.g.*, tensile reflections leading to spall failure. Fully resolved methods must be used to account

for heterogeneous microstructures and for quasi-longitudinal and quasi-transverse waves that arise in low symmetry crystal orientations.

3.3. Dynamic Finite Element Analysis of Microstructures

Unlike the models of planar shock propagation evaluated in § 3.1 and § 3.2, wherein geometries of the solid are restricted to a single space dimension (*i.e.*, 1-D), in fully resolved dynamic calculations of §3.3, the geometry may be 2-D or 3-D. Furthermore, morphology of microstructure---grain sizes, grain shapes, grain boundaries, secondary phases at grain boundaries, and so forth---are now resolved explicitly. Geometric rendering of complex polycrystalline geometries via finite elements is non-trivial, with the procedure described for polyhedral grains, for example, in [81, 82] and references therein.

The present focus is on models wherein single crystals within each polycrystal are resolved explicitly, as represented in crystal elastic or elastic-plastic simulations of realistic microstructures [54, 83, 81, 84, 85, 86]. The constitutive models for response of the material in a dynamic finite element context are a subset of the general class of nonlinear continuum thermomechanics models discussed in §3.3. For single crystals that undergo plastic deformation, the plastic velocity gradient is the sum of contributions of slip rates $\dot{\gamma}^{\alpha}$, where the superscript denotes a slip system for dislocation glide with direction $\boldsymbol{s}^{\alpha}$ and plane normal $\boldsymbol{m}^{\alpha}$:

$$\boldsymbol{L}^{P} = \dot{\boldsymbol{F}}^{P}\boldsymbol{F}^{P-1} = \sum_{\alpha} \dot{\gamma}^{\alpha}\boldsymbol{s}^{\alpha} \otimes \boldsymbol{m}^{\alpha}. \tag{3.5}$$

The slip direction and slip plane normal are orthogonal and of unit length, *i.e.*, are those of the crystal lattice prior to thermoelastic deformation. Denoting the resolved shear stress acting on a system by τ^{α}, the flow rule for slip rates is

$$\dot{\gamma}_{\alpha} = \dot{\gamma}_{\alpha}(\tau^{\alpha}, T, \{\xi\}),\ \tau^{\alpha} = J^{E}\boldsymbol{\sigma}\colon[\boldsymbol{F}^{E}\boldsymbol{s}^{\alpha} \otimes (\boldsymbol{F}^{E})^{-\mathrm{T}}\boldsymbol{m}^{\alpha}]. \tag{3.6}$$

When regions of very large defect density are encountered, (2.22) may be insufficient when $\boldsymbol{F}^{P}$ is attributed to dislocation slip processes alone as in (3.5). An intermediate term, denoted here by $\boldsymbol{F}^{I}$, can be used to quantify residual lattice deformation due to defects within the local volume to which (2.22) is assigned:

$$\boldsymbol{F} = \nabla_{0}\boldsymbol{x} = \boldsymbol{F}^{E}\boldsymbol{F}^{I}\boldsymbol{F}^{P}. \tag{3.7}$$

Here it is assumed that damage is absent within the single crystal; otherwise, $\boldsymbol{F}^{D}$ may be appended to the right side of (3.7). The particular form of $\boldsymbol{F}^{I}$ depends on the class of defect, defect arrangement, and scale of resolution, as derived via a number of theoretical methods, [83, 87, 88, 89, 90, 91, 92, 17]. Analysis has demonstrated the importance of inclusion of $\boldsymbol{F}^{I}$ in the constitutive description when dislocation densities approach the theoretical maximum, which is possible for severe plastic deformation or shock loading [73, 91]. Since $\boldsymbol{F}^{P}$ is isochoric when attributed solely to slip, any residual volume changes in the crystal are omitted if not captured by $\boldsymbol{F}^{I}$. Lattice rotations induced by disclinations may be described by rotational part of $\boldsymbol{F}^{I}$ [93], and volume changes associated with point defects such as vacancies or interstitial atoms may incorporated as well [94, 95].

Also not addressed explicitly in equations herein is the possibility of deformation twinning. This phenomenon is observed in many kinds of crystals deformed at high loading rates, especially those of lower symmetry and low stacking fault energy. Models invoking pseudo-slip kinetics [96, 97, 73, 98, 99, 75] or phase field descriptions [100, 101, 102, 103, 104] have been implemented in numerical simulations of twinning processes in single crystals and polycrystals. Phase transformations can likewise be included via diffuse interface modeling [105] or other prescribed criteria in continuum frameworks. An example result of a dynamic polycrystal simulation incorporating the latter is shown in Fig. **3** of [86], wherein the crystal-to-glass solid-solid transformation in shocked boron carbide is modeled via an intrinsic nonlinear elastic instability criterion [106, 107]. Quantitative data from 3-D simulations demonstrating validity of the continuum theory for boron carbide versus planar impact experiments are shown in Fig. **4**(**a**) of [86], with further comparisons to various analytical, atomic, and experimental results listed in Table **4** of that reference.

Cohesive fracture models are now a standard representation of failure of the material at the mesoscale, *i.e.*, the length scale of polycrystalline microstructures of the order of the grain size. The first explicit dynamics simulations coupling finite crystal plasticity with cohesive failure seem to be those reported in [54, 84] with a follow-up study of spall in [20]. Key equations, in generic forms, for cohesive fracture models of the sort implemented in spall fracture simulations such as that in Fig. **5** of [84] and others in [20, 21] are reviewed in what follows next. Quantitative comparison of cohesive finite element results with spall fracture experiments is obtained by inspection of Figs. **10** and **26** of [20].

Let the crack opening displacement vector across two crack faces initially coincident at point $\boldsymbol{X}$ be defined as the displacement jump

$$\boldsymbol{\delta}(\boldsymbol{X}, t) = [[\boldsymbol{u}(\boldsymbol{X}, t)]], \tag{3.8}$$

where displacement $\boldsymbol{u}$ need be continuous with respect to position only within regions of the body that have not undergone fracture. The unit vector $\boldsymbol{n}(\boldsymbol{X})$ is normal to the surface of impending fracture. Let $\boldsymbol{t}_{0}$ denote the traction vector per unit reference area:

$$\boldsymbol{t}_{0} = \boldsymbol{P} \cdot \boldsymbol{n}, \tag{3.9}$$

with $\boldsymbol{P} = (\rho/\rho_{0})\boldsymbol{\sigma}\boldsymbol{F}^{-\mathrm{T}}$ the first Piola-Kirchhoff stress. A traction-separation law is prescribed in the cohesive zone of a generic functional form:

$$\boldsymbol{t}_{0} = \boldsymbol{t}_{0}(\boldsymbol{\delta}, \{\chi\}). \tag{3.10}$$

Possible history effects are addressed by state variable(s) $\{\chi\}$. A magnitude of displacement δ_{C} is usually assigned as a material property, beyond which traction vanishes and the formerly cohesive surfaces become free surfaces. For simulations invoking explicit numerical integration, a stiffness matrix is usually not needed, in which case the traction function need not have a continuous derivative with respect to opening displacement. The work done during separation can be related to a surface energy of fracture Υ:

$$\Upsilon = \frac{1}{2}\int_0^{\delta_C} \boldsymbol{t}_0 \cdot \mathrm{d}\boldsymbol{\delta}, \tag{3.11}$$

where the path of integration ends when the critical separation magnitude is attained. A commonly used model is the triangular cohesive degradation function

$$|t_0| = \sigma_C\left(1-|\boldsymbol{\delta}|/\delta_C\right) \ |\vec{t}_0| = \sigma_C(1-|\boldsymbol{\delta}|/\delta_C). \tag{3.12}$$

This law can be invoked separately for each magnitude $|\cdot|$ of normal and shear components of traction and opening displacement. The resolved scalar stress component at which the cohesive zone starts to open is σ_C, *i.e.*, is the strength required to initiate fracture or separation. Only two of the three parameters Υ, σ_C, and δ_C must be assigned since (3.11) eliminates one of these algebraically. More sophisticated models accounting for mode mixity and other physical behaviors have been implemented [108, 109] but often at the cost of additional calibration or parameters.

Cohesive failure models allow for realistic modeling of dynamic failure of microstructures, including crack speeds, branching, and stress wave interactions. Crack sizes and shapes are fully resolved. Positives of this class of model include relatively few parameters [minimally two, *e.g.*, δ_C and σ_C in the context of (3.12)] and distinct behavior of interfaces and bulk material, meaning that traditional solid continuum elements can be used for representing the latter. However, more parameters are needed to account for distributions of strengths and surface energies among potential failure sites in more realistic simulations of heterogeneous materials. Anisotropy and nonlinearity of the bulk crystal response can be incorporated via the physically rigorous theory outlined in §2.3 and earlier in §3.3.

Compared to analytical solutions to the Rankine-Hugoniot jump conditions of §3.1, or to numerical solutions to the 1-D equations of motion under the steady wave assumption in § 3.2, explicit dynamics calculations are obtained at very high expense. Mesh generation procedures for realistic microstructures are often tedious and cumbersome, implementation of complex anisotropic elastic-plastic constitutive models is difficult, and integration of the governing equations of nonlinear continuum mechanics in conjunction with the equations of these constitutive models is computationally costly. As remarked already in §2.3, the Courant condition setting the maximum time step size becomes prohibitive for very small element sizes which in turn are unavoidable for modeling of polycrystals of grain dimensions on the order of a few micrometers or less. On the other hand, the reduced order (1-D) models in §3.1 and §3.2, while enabling sophisticated constitutive models for single crystals or homogenized polycrystals with overall textures, do not account for details of microstructure morphology. Grain sizes, grain shapes, and grain boundary geometries are all omitted, as are failure entities such as discrete fracture planes, individual voids, and distinct adiabatic shear bands. In contrast, all of these effects are potentially included in fully resolved calculations of §3.3. Thus, only the latter fully resolved calculations offer the possibility of optimization of materials at the micro- or mesoscale for improved performance (*e.g.*, ballistic penetration resistance). Furthermore, such calculations may serve as a source of fundamental functional forms and/or material parameters for constitutive model equations invoked at higher length scales. See for example [54, 14, 15, 81] for examples of this sequential multiscale approach applied to metals and ceramics for protection applications.

Numerical implementation of cohesive models is deemed straightforward, but additional nodal degrees of freedom increase the computational expense where duplicate nodes are inserted along failure planes. A limitation is that fracture paths are constrained to follow element boundaries. When fractures are restricted to pre-existing interfaces such as grain or phase boundaries, cohesive finite elements can be seeded a priori along such pending failure surfaces. Cleavage fracture on specific planes can also be depicted [110]. Extremely fine meshes are often necessary for representing the small fracture process zones of materials with high strength and low surface energy; see for example the spall simulations of polycrystalline silicon carbide in [21]. Another class of models used to represent fracture of microstructures, not considered further here, invokes the phase field (*i.e.*, diffuse interface) concept [111, 112, 113, 82, 114] in contrast to the sharp interface assumption inherent in the cohesive finite element method.

4. CURRENT AND FUTURE DEVELOPMENTS

Current modeling techniques describing two kinds of physical problem---ballistic penetration and planar shock wave propagation---have been presented and compared. For each kind of problem, models have been categorized as analytical, reduced order, or fully resolved. Perspectives on relative complexity, generality, and phenomenology are summarized in Table **1**. Trends are an increase in flexibility (*i.e.*, increased fidelity of physical description) with increasing complexity/sophistication, albeit usually at the

Table 1. Classes of impact mechanics models, examples, and general characteristics.

	Analytical (1-D)	**Reduced Order (1-D)**	**Fully Resolved Dynamics (2-D or 3-D)**
Examples: penetration mechanics	Bernoulli hydrodynamics	Extended hydrodynamics	Hydrocode simulations
Examples: planar impact	Hugoniot solutions	Steady wave analysis	Explicit finite element simulations
Complexity (usual governing equations)	Low	Moderate	High
Generality (usual physics addressed)	Low	Moderate	High
Phenomenology (typical calibration and parameters)	Low	High	Moderate

expense of increasing number of fitted parameters or equations. These trends are general, and exceptions of course are possible.

It is emphasized that only the fully resolved dynamic simulations, though computationally costly, are able to provide insight into effects of fine scale microstructures of materials involved. Such effects are implicitly embedded within parameters entering reduced order and analytical treatments, but their origins are not evident in such cases, thus prohibiting computationally driven materials design. In contrast, modern simulations at multiple length and time scales are becoming increasingly important in development and optimization of advanced functional materials for high rate applications such as those related to terminal ballistics. Future developments will advance such material system design via computer simulations.

CONFLICT OF INTEREST

The author reports no conflict of interest and received no payment for preparation of this manuscript.

ACKNOWLEDGEMENT

This paper was written while the author served as a visiting research fellow at Columbia University, specifically in the Department of Civil Engineering and Engineering Mechanics of the Fu Foundation School of Engineering and Applied Science in New York, NY, USA. The author acknowledges the courtesy of Dr. WaiChing (Steve) Sun for hosting his sabbatical visit at Columbia University in 2016.

REFERENCES

[1] M. Meyers, Dynamic Behavior of Materials. New York: Wiley, 1994.

[2] R. Alderliesten, "On the development of hybrid material concepts for aircraft structures," *Recent Pat. Eng.*, Vol. 3, pp.25–38, 2009.

[3] V. Carandente, and R. Savino, "New concepts of deployable de-orbit and re-entry systems for CubeSat miniaturized satellites," *Recent Pat. Eng*, Vol. 8, pp.2–12, 2014.

[4] L. Olovsson, "*Eulerian-lagrangian mapping for finite element analysis*," U.S. Patent 7,167,816, 2007.

[5] A. G. Baxter, R. Jones, and T. Stuart, "*Ceramic armour element for use in armour,*" U.S. Patent 8,833,229, 2014.

[6] Y. Kucherov, G. Hubler, and B. Johnson, "*Armor plate with shock wave absorbing properties,*" U.S. Patent 8,695,476, 2014.

[7] Z. Rosenberg, and E. Dekel, Terminal Ballistics. Berlin: Springer, 2012.

[8] M. Backman and W. Goldsmith, "The mechanics of penetration of projectiles into targets," *Int. J. Eng. Sci*., Vol. 16, pp.1–99, 1978.

[9] J. Zukas, High Velocity Impact Dynamics. New York: Wiley-Interscience, 1990.

[10] J. Clayton, "Penetration resistance of armor ceramics: dimensional analysis and property correlations," *Int. J. Impact Eng*., Vol. 85, pp. 124–131, 2015.

[11] J. Clayton, "Dimensional analysis and extended hydrodynamic theory applied to long-rod penetration of ceramics," *Defence Tech*., Vol. 12, pp.334–342, 2016.

[12] C. Anderson, and J. Riegel, "A penetration model for metallic targets based on experimental data," *Int. J. Impact Eng*., Vol. 80, pp.24–35, 2015.

[13] J. Riegel, and D. Davison, "Consistent constitutive modeling of metallic target penetration using empirical, analytical, and numerical penetration models," *Defence Tech*., Vol. 12, pp.202–214, 2016.

[14] J. Clayton, "Modeling effects of crystalline microstructure, energy storage mechanisms, and residual volume changes on penetration resistance of precipitate-hardened aluminum alloys," *Compos. B: Eng.*, Vol. 40, pp.443–450, 2009.

[15] J. Clayton, "Two-scale modeling of effects of microstructure and thermomechanical properties on the dynamic performance of an aluminum alloy," *Int. J. Materials and Structural Integrity*, Vol. 4, pp.116–140, 2010.

[16] J. Clayton, "Modeling and simulation of ballistic penetration of ceramic-polymer-metal layered systems," *Math. probl. eng*, vol. 2015, p. 709498, 2015.

[17] J. Clayton, Nonlinear Mechanics of Crystals. Dordrecht: Springer, 2011.

[18] T. Antoun, Spall Fracture. New York: Springer, 2003.

[19] R. Kinslow, High-velocity Impact Phenomena. New York: Academic Press, 1970.

[20] T. Vogler and J. Clayton, "Heterogeneous deformation and spall of an extruded tungsten alloy: plate impact experiments and crystal plasticity modeling," *J. Mech. Phys. Solids*, Vol. 56, pp.297–335, 2008.

[21] J. Foulk, and T. Vogler, "A grain-scale study of spall in brittle materials," Int. J. Fracture, Vol. 163, pp.225–242, 2010.

[22] D. Wallace, Statistical Physics of Crystals and Liquids: a Guide to Highly Accurate Equations of State. Singapore: World Scientific, 2003.

[23] J. Clayton, and A. Tonge, "A nonlinear anisotropic elastic-inelastic constitutive model for polycrystalline ceramics and minerals with application to boron carbide," *Int. J. Solids. Struct.*, Vol. 64–65, pp.191–207, 2015.

[24] G. Birkhoff, D. MacDougall, E. Pugh, and G. Taylor, "Explosives with lined cavities," *J. Appl. Phys.,* vol. 19, pp.563–582, 1948.

[25] W. Herrmann, and J. Wilbeck, "Review of hypervelocity penetration theories," *Int. J. Impact Eng*., Vol. 5, pp.307–322, 1987.

[26] D. Pack, and W. Evans, "Penetration by high-velocity ('Munroe') jets: I," *Proc. Phys. Soc. B*, Vol. 64, pp.298–302, 1951.

[27] W. Evans, and D. Pack, "Penetration by high-velocity ('Munroe') jets: II," *Proc. Phys. Soc. B*, Vol. 64, pp.303–310, 1951.

[28] R. Eichelberger, "Experimental test of the theory of penetration by metallic jets," *J. Appl. Phys*. Vol. 27, pp.63–68, 1956.

[29] V. Alekseevskii, "Penetration of a rod into a target at high velocity," *Combust. Explos. Shock Waves*, Vol. 2, pp.63–66, 1966.

[30] A. Tate, "A theory for the deceleration of long rods after impact," *J. Mech. Phys. Solids*, Vol. 15, pp.387–399, 1967.

[31] W. Walters, and S. Segletes, "An exact solution of the long rod penetration equations," *Int. J. Impact Eng*., Vol. 11, pp.225–231, 1991.

[32] C. Anderson and J. Walker, "An examination of long-rod penetration," *Int. J. Impact Eng*, Vol. 11, pp.481–501, 1991.

[33] J. Walker and C. Anderson, "A time-dependent model for long-rod penetration," *Int. J. Impact Eng*, Vol. 16, pp.19–48, 1995.

[34] C. Anderson, S. Mullin, and C. Kuhlman, "Computer simulation of strain-rate effects in replica scale model penetration experiments," *Int. J. Impact Eng*, Vol. 13, pp.35–52, 1993.

[35] C. Anderson, S. Mullin, A. Piekutowski, N. Blaylock, and K. Poormon, "Scale model experiments with ceramic laminate targets," *Int. J. Impact Eng*, Vol. 18, pp.1–22, 1996.

[36] C. Anderson, D. Orphal, R. Franzen, and J. Walker, "On the hydrodynamic approximation for long-rod penetration," *Int. J. Impact Eng*, Vol. 22, pp.23–43, 1999.

[37] C. Anderson and D. Orphal, "An examination of deviations from hydrodynamic penetration theory," *Int. J. Impact Eng*, Vol. 35, pp.1386–1392, 2008.

[38] J. Clayton, "A model for deformation and fragmentation in crushable brittle solids *Int. J. Impact Eng*, Vol. 35, pp.269–289, 2008.

[39] J. Clayton, "Deformation, fracture, and fragmentation in brittle geologic solids," *Int. J. Fracture*, Vol. 163, pp.151–172, 2010.

[40] R. Subramanian, and S. Bless, "Penetration of semi-infinite AD995 alumina targets by tungsten long rod penetrators from 1.5 to 3.5 km/s," *Int. J. Impact Eng*, Vol. 17, pp.807–816, 1995.

[41] D. Orphal, R. Franzen, A. Piekutowski, and M. Forrestal, "Penetration of confined aluminum nitride targets by tungsten long rods at 1.5–4.5 km/ s," *Int. J. Impact Eng*, Vol. 18, pp.355–368, 1996.

[42] D. Orphal and R. Franzen, "Penetration of confined silicon carbide targets by tungsten long rods at impact velocities from 1.5 to 4.6 km/s," *Int. J. Impact Eng*, Vol. 19, pp.1–13, 1997.

[43] D. Orphal, R. Franzen, A. Charters, T. Menna, and A. Piekutowski, "Penetration of confined boron carbide targets by tungsten long

rods at impact velocities from 1.5 to 5.0 km/s *Int. J. Impact Eng*, Vol. 19, pp.15–29, 1997.

[44] S. Savio, K. Ramanjaneyulu, V. Madhu, and T. Bhat, "An experimental study on ballistic performance of boron carbide tiles," *Int. J. Impact Eng*, Vol. 38, pp.535–541, 2011.

[45] J. Reaugh, A. Holt, M. Wilkins, B. Cunningham, B. Hord, and A. Kusubov, "Impact studies of five ceramic materials and pyrex," *Int. J. Impact Eng*, Vol. 23, pp.771–782, 1999.

[46] F. Roters, P. Eisenlohr, L. Hantcherli, D. Tjahjanto, T. Bieler, and D. Raabe, "Overview of constitutive laws, kinematics, homogenization and multiscale methods in crystal plasticity finite-element modeling: Theory, experiments, applications," *Acta Mater*., Vol. 58, pp.1152–1211, 2010.

[47] J. Clayton, "Nonlinear Eulerian thermoelasticity for anisotropic crystals," *J. Mech. Phys. Solids*, Vol. 61, pp.1983–2014, 2013.

[48] J. Clayton, "Analysis of shock compression of strong single crystals with logarithmic thermoelastic-plastic theory*," Int. J. Eng. Sci.,* Vol. 79, pp.1–20, 2014.

[49] J. Clayton, Differential Geometry and Kinematics of Continua. Singapore: World Scientific, 2014.

[50] R. Thurston, "Waves in solids," in Handbuch der Physik, Vol. 4, (Berlin), pp.109–308, Springer, 1974.

[51] C. Teodosiu, Elastic Models of Crystal Defects. Berlin: Springer, 1982.

[52] D. Bammann, and K. Solanki, "On kinematic, thermodynamic, and kinetic coupling of a damage theory for polycrystalline material," *Int. J. Plasticity*, Vol. 26, pp.775–793, 2010.

[53] G. Del Piero, and D. Owen, "Structured deformations of continua," *Arch. Rational Mech. Anal*., vol. 124, pp. 99–155, 1993.

[54] J. Clayton, "Dynamic plasticity and fracture in high density polycrystals: constitutive modeling and numerical simulation," *J. Mech. Phys. Solids*, Vol. 53, pp.261–301, 2005.

[55] J. Clayton, "Continuum multiscale modeling of finite deformation plasticity and anisotropic damage in polycrystals," *Theor. Appl. Fract. Mec*., Vol. 45, pp.163–185, 2006.

[56] J. Clayton, and D. McDowell, "Finite polycrystalline elastoplasticity and damage: multiscale kinematics," *Int. J. Solids Struct*., Vol. 40, pp.5669–5688, 2003.

[57] J. Clayton, and D. McDowell, "Homogenized finite elastoplasticity and damage: theory and computations," *Mech Mater*., Vol. 36, pp.799–824, 2004.

[58] D. Bammann, and E. Aifantis, "A damage model for ductile metals," *Nucl. Eng. Des*., Vol. 116, pp.355–362, 1989.

[59] O. Aslan, N. Cordero, A. Gaubert, and S. Forest, "Micromorphic approach to single crystal plasticity and damage," *Int. J. Eng. Sci.,* vol. 49, pp.1311–1325, 2011.

[60] J. Clayton, "Shock compression of metal crystals: a comparison of Eulerian and Lagrangian elastic-plastic theories," *Int. J. Appl. Mech*., Vol. 6, pp.1450048, 2014.

[61] J. Clayton, "Defects in nonlinear elastic crystals: differential geometry, finite kinematics, and second-order analytical solutions," *Appl.Math. Mech.* Vol. 95, pp.476–510, 2015.

[62] J. Clayton, "Crystal thermoelasticity at extreme loading rates and pressures: analysis of higher-order energy potentials," *Extreme Mech. Lett.*, Vol. 3, pp.113–122, 2015.

[63] J.-H. Song, H. Wang, and T. Belytschko, "A comparative study on finite element methods for dynamic fracture," *Comput. Mech*., Vol. 2, pp.239–250, 2008.

[64] G. Johnson, and R. Stryk, "Conversion of 3D distorted elements into meshless particles during dynamic deformation," *Int. J. Impact Eng*., Vol. 28, pp.947–966, 2003.

[65] G. Zi, H. Chen, J. Xu, and T. Belytschko, "The extended finite element method for dynamic fractures," *Shock Vib*., Vol. 12, pp.9–23, 2005.

[66] F. Kun, and H. Herrmann, "A study of fragmentation processes using a discrete element method," *Comput. methods Appl. Mech. Eng*. Vol. 138, pp.3–18, 1996.

[67] S. Yadav, and G. Ravichandran, "Penetration resistance of laminated ceramic/polymer structures," *Int. J. Impact Eng*., Vol. 28, pp. 557–574, 2003.

[68] J. Lloyd, J. Clayton, R. Austin, and D. McDowell, "Shock compression modeling of metallic single crystals: comparison of finite difference, steady wave, and analytical solutions," *Adv. Model. Simulat. Eng. Sci.*, Vol. 2, pp. 14, 2015.

[69] P. Germain, and E. Lee, "On shock waves in elastic-plastic solids," *J. Mech. Phys. Solids*, Vol. 21, pp.359–382, 1973.

[70] R. Courant and K. Friedrichs, Supersonic flow and shock waves. New York: Springer, 1999.

[71] G. Perrin, and M. Delannoy-Coutris, "Analysis of plane elastic-plastic shock-waves from the fourth-order anharmonic theory," *Mech. Mater*., Vol. 2, pp.139–153, 1983.

[72] J. Clayton, "Finite strain analysis of shock compression of brittle solids applied to titanium diboride," *Int. J. Impact Eng*., Vol. 73, pp.56–65, 2014.

[73] J. Clayton, "A continuum description of nonlinear elasticity, slip and twinning, with application to sapphire," *Proc. R. Soc. Lond. A*, Vol. 465, pp.307–334, 2009.

[74] J. Clayton, "Modeling nonlinear electromechanical behavior of shocked silicon carbide," *J. Appl. Phy*., Vol. 107, pp.013520, 2010.

[75] J. Clayton, "A nonlinear thermomechanical model of spinel ceramics applied to aluminum oxynitride (AlON)," *J. Appl. Mech*., Vol. 78, pp.011013, 2011.

[76] A. Molinari and G. Ravichandran, "Fundamental structure of steady plastic shock waves in metals," *J. Appl. Phys*. Vol. 95, pp.1718–1732, 2004.

[77] R. Austin, and D. McDowell, "A dislocation-based constitutive model for viscoplastic deformation of FCC metals at very high strain rates," *Int. J. Plasticity*, Vol. 27, pp.1–24, 2011.

[78] J. Lloyd, J. Clayton, R. Austin, and D. McDowell, "Plane wave simulation of elastic-viscoplastic single crystals," *J. Mech. Phys. Solids*, Vol. 69, pp.14–32, 2014.

[79] J. Lloyd, J. Clayton, R. Austin, and D. McDowell, "Modeling single-crystal microstructure evolution due to shock loading," *J. Phys.: Conference Series*, Vol. 500, pp.112040, 2014.

[80] J. Lloyd, J. Clayton, R. Becker, and D. McDowell, "Simulation of shock wave propagation in single crystal and polycrystalline aluminum," *Int. J. Plasticity*, Vol. 60, pp.118–144, 2014.

[81] J. Clayton, R. Kraft, and R. Leavy, "Mesoscale modeling of nonlinear elasticity and fracture in ceramic polycrystals under dynamic shear and compression," *Int. J. Solids and Struct*., Vol. 49, pp. 2686–2702, 2012.

[82] J. Clayton, and J. Knap, "Phase field modeling of directional fracture in anisotropic polycrystals," *Comp. Mater*. Sci.,Vol.98, pp.158–169, 2015.

[83] J. Clayton, and D. McDowell, "A multiscale multiplicative decomposition for elastoplasticity of polycrystals," *Int. J. Plasticity*, Vol. 19, pp.1401–1444, 2003.

[84] J. Clayton, "Modeling dynamic plasticity and spall fracture in high density polycrystalline alloys," *Int. J. Solids Struct*., Vol. 42, pp.4613–4640, 2005.

[85] J. Clayton, "Plasticity and spall in high density polycrystals: modeling and simulation," in Shock Compression of Condensed Matter (M. Furnish, M. Elert, T. Russell, and C. White, eds.), Vol. 845, pp.311–314, AIP Conference Proceedings, 2006.

[86] J. Clayton, "Mesoscale modeling of dynamic compression of boron carbide polycrystals," *Mech. Res. Commun*., Vol. 49, pp.57–64, 2013.

[87] J. Clayton, D. McDowell, and D. Bammann, "A multiscale gradient theory for elastoviscoplasticity of single crystals," *Int. J. Eng. Sci*., vol. 42, pp. 427–457, 2004.

[88] J. Gerken, and P. Dawson, "A crystal plasticity model that incorporates stresses and strains due to slip gradients," *J. Mech. Phys. Solids*, Vol. 56, 2008.

[89] D. Luscher, J. Mayeur, H. Mourad, A. Hunter, and M. Kenamond, "Coupling continuum dislocation transport with crystal plasticity for application to shock loading conditions *Int. J. Plasticity*, Vol. 76, pp.111–129, 2016.

[90] J. Clayton, C. Hartley, and D. McDowell, "The missing term in the decomposition of finite deformation," *Int. J. Plasticity*, Vol. 52, pp.51–76, 2014.

[91] J. Clayton, "An alternative three-term decomposition for single crystal deformation motivated by non-linear elastic dislocation solutions," *J. Mech. Appl. Math*., Vol. 67, pp.127–158, 2014.

[92] J. Clayton, and D. Bammann, "Finite deformations and internal forces in elastic-plastic crystals: interpretations from nonlinear elasticity and anharmonic lattice statics," *J. Eng. Mater. Technol.*, Vol. 131, pp.041201, 2009.

[93] J. Clayton, D. McDowell, and D. Bammann, "Modeling dislocations and disclinations with finite micropolar elastoplasticity*," Int. J. Plasticity*, Vol. 22, pp.210–256, 2006.

[94] J. Clayton, D. Bammann, and D. McDowell, "A geometric framework for the kinematics of crystals with defects," Philosophical Magazine, vol. 85, pp. 3983–4010, 2005.

[95] J. Clayton, "A non-linear model for elastic dielectric crystals with mobile vacancies," *Int. J. Non Linear Mech.,* Vol. 44, pp. 675–688, 2009.

[96] S. Kalidindi, "Incorporation of deformation twinning in crystal plasticity models," *J. Mech. Phys. Solids*, Vol. 46, pp.267–290, 1998.

[97] A. Staroselsky, and L. Anand, "Inelastic deformation of polycrystalline face centered cubic materials by slip and twinning," *J. Mech. Phys. Solids*, Vol. 46, pp.671–696, 1998.

[98] N. Barton, N. Winter, and J. Reaugh, "Defect evolution and pore collapse in crystalline energetic materials," *Model. Simul. Mater. ScI. Eng*., Vol. 17, pp.035003, 2009.

[99] J. Clayton, "Modeling finite deformations in trigonal ceramic crystals with lattice defects," *Int. J. Plasticity*, Vol. 26, pp.1357–1386, 2010.

[100] J. Clayton, and J. Knap, "A phase field model of deformation twinning: nonlinear theory and numerical simulations," *Physica D*, Vol. 240, pp.841–858, 2011.

[101] J. Clayton, and J. Knap, "Phase field modeling of twinning in indentation of transparent single crystals," *Model. Simul. Mater. ScI. Eng*., Vol. 19, pp.085005, 2011.

[102] F. Hildebrand and C. Miehe, "A phase field model for the formation and evolution of martensitic laminate microstructure at finite strains," *Philos. Mag*., Vol. 92, pp.4250–4290, 2012.

[103] J. Clayton and J. Knap, "Phase field analysis of fracture induced twinning in single crystals," *Acta Mater*, Vol. 61, pp.5341–5353, 2013.

[104] J. Clayton and J. Knap, "Phase field modeling of coupled fracture and twinning in single crystals and polycrystals," *Comp. Methods Appl. Mech. Eng.*, in press, 2016.

[105] J. Clayton, "Phase field theory and analysis of pressure-shear induced amorphization and failure in boron carbide ceramic," *AIMS Mater. Sci.,* Vol. 1, pp.143–158, 2014.

[106] J. Clayton, "Towards a nonlinear elastic representation of finite compression and instability of boron carbide ceramic," *Philos. Mag*., Vol. 92, pp.2860–2893, 2012.

[107] J. Clayton, and K. Bliss, "Analysis of intrinsic stability criteria for isotropic third-order green elastic and compressible neo-Hookean solids," *Mech. Mater.,* Vol. 68, pp.104–119, 2014.

[108] X.-P. Xu and A. Needleman, "Numerical simulations of fast crack growth in brittle solids," *J. Mech. Phys. Solids*, Vol. 42, pp.1397–1434, 1994.

[109] H. Espinosa, and P. Zavattieri, "A grain level model for the study of failure initiation and evolution in polycrystalline brittle materials. Part II: Numerical examples," *Mech. Mater*., Vol. 35, pp.365–394, 2003.

[110] R. Kraft, and J. Molinari, "A statistical investigation of the effects of grain boundary properties on transgranular fracture," *Acta Mater.*, Vol. 56, pp. 4739–4749, 2008.

[111] Y. Jin, Y. Wang, and A. Khachaturyan, "Three-dimensional phase field microelasticity theory and modeling of multiple cracks and voids," *Appl. Phys. Lett*., Vol. 79, pp.3071–3073, 2001.

[112] A. Karma, D. Kessler, and H. Levine, "Phase-field model of mode III dynamic fracture," *Phys. Rev. Lett*., Vol. 87, pp.045501, 2001.

[113] J. Clayton, and J. Knap, "A geometrically nonlinear phase field theory of brittle fracture," *Int. J. Fracture*, Vol. 189, pp.139–148, 2014.

[114] J. Clayton and J. Knap, "Nonlinear phase field theory for fracture and twinning with analysis of simple shear," *Philos. Mag*., Vol. 95, pp.2661–2696, 2015.

1 (PDF) DEFENSE TECHNICAL INFORMATION CTR DTIC OCA

2 (PDF) DIRECTOR US ARMY RESEARCH LAB RDRL CIO L IMAL HRA MAIL & RECORDS MGMT

1 (PDF) GOVT PRINTG OFC A MALHOTRA

47 (PDF) DIR USARL
RDRL CIH C
J KNAP
RDRL DP
T BJERKE
RDRL WM
B FORCH
S KARNA
J MCCAULEY
J ZABINSKI
S SCHOENFELD
RDRL WML B
I BATYREV
R PESCE-RODRIGUEZ
B RICE
D TAYLOR
N WEINGARTEN
RDRL WML H
B AYDELOTTE
D MALLICK
C MEYER
B SCHUSTER
RDRL WMM
J BEATTY
RDRL WMM B
G GAZONAS
D HOPKINS
B LOVE
B POWERS
R WILDMAN
RDRL WMM E
J LASALVIA
J SWAB
RDRL WMM F
E HERNANDEZ
T SANO
M TSCHOPP
RDRL WMM G
J ANDZELM
RDRL WMP A
S BILYK
RDRL WMP B
C HOPPEL
J MCDONALD
S SATAPATHY
M SCHEIDLER
T WEERISOORIYA
RDRL WMP C
R BECKER
D CASEM
J CLAYTON
M FERMEN-COKER
M GREENFIELD
R LEAVY
J LLOYD
S SEGLETES
A TONGE
C WILLIAMS
A SOKOLOW
RDRL WMP D
R DONEY
C RANDOW